Composites Science and Technology 246 (2024) 110388

Contents lists available at ScienceDirect

Composites Science and Technology

journal homepage: www.elsevier.com/locate/compscitech

Transfer-learning-based strategy for enhancing prediction accuracy and computational efficiency of nonlinear mechanical properties in composite materials

Chenyu Nan, Hongshi Ruan, Xiaozhe Ju, Junhan Hu, Lihua Liang, Yangjian Xu *

College of Mechanical Engineering, Zhejiang University of Technology, Hangzhou 310023, China

ARTICLE INFO

Keywords:
Reduced order model
Transfer learning
Composites
Nonlinear
Homogenization

ABSTRACT

In modern composite design, superior macroscopic mechanical properties can be achieved by optimizing the microstructures of materials. However, the direct prediction of the microstructure–property relationship under nonlinear conditions through numerical methods can be inefficient or imprecise. In this study, a transfer learning strategy based on the reduced order model (ROM) was proposed, offering an enhanced and rapid prediction of the mechanical responses of composite materials under nonlinear conditions. Initially, an extensive training dataset was generated by applying the ROM, used to pre-train the neural network model. Following this, a few data calculated from full-order finite element models were leveraged to fine-tune the network parameters. This approach exploits the efficient data generation capability of the ROM, with its potential computational inaccuracies in nonlinear scenarios mitigated, leading to an improvement in the accuracy and efficiency of the surrogate model. Numerical examples of a nonlinear hyper-elastic material with inclusions were examined, revealing that the computational cost in the offline stage of the transfer learning method is only half that of traditional neural network models, and it enable near real-time predictions in the online stage. Notably, it was shown that the accuracy loss of the developed surrogate model in scenarios of strong non-linearity is significantly less than that of the ROM. This method presents an innovative pathway for the swift and accurate evaluation of the effective mechanical properties of composite structures, with the potential to offer valuable insights for related methodological research.

1. Introduction

As modern materials face growing demands for enhanced performance, reliability, and cost-efficiency, the study of composite materials has received significant attention due to their exceptional properties. Consequently, an increasing number of researchers are devoting their efforts to exploring innovative design methodologies. One of the fundamental goals of composite material design lies in augmenting the macroscopic mechanical response of the material through sophisticated microstructure design. If the correlation between microstructural characteristics and macro-scale effective mechanical properties can be effectively delineated, it will not only expedite simulations of composite materials with complex microstructures, but also facilitate a deeper understanding of how interactions among different microstructural components affect macroscopic properties. Ultimately, this understanding could propel the discovery and design of next-generation composite materials.

At present, the study of the mechanical properties of composite materials is primarily dominated by homogenization methods [1–3]. For linear multiphase composites with simplistic microstructures, a variety of effective techniques have been established. However, these homogenization methods confront significant challenges when addressing nonlinear issues [4–7], such as nonlinear elasticity, elastoplasticity, viscoelasticity, and creep, particularly in the context of path-dependent problems [8]. Analytical methods can yield satisfactory results when applied to scenarios with relatively simplistic microstructures and material characteristics. However, they tend to be inadequate when faced with complex microstructures or sophisticated material behaviors, such as localized plastic deformation. As a result, researchers typically opted for a suitable representative volume element (RVE), upon which numerical models were constructed to probe and delineate the macroscopic mechanical properties of materials. Given that the RVE model statistically echoes the microstructural morphology of the composite material, it can provide a precise representation of the composite's macroscopic mechanical properties.

The finite element method (FEM) is a widely employed numerical technique in the field of composite materials science due to its broad applicability [9]. In this method, the RVE is discretized, and

* Corresponding author.
E-mail address: xuyangjian571@163.com (Y. Xu).

https://doi.org/10.1016/j.compscitech.2023.110388
Received 26 August 2023; Received in revised form 27 November 2023; Accepted 6 December 2023
Available online 8 December 2023

periodic boundary conditions are defined. Subsequently, the RVE equilibrium equation, which satisfies the Hill–Mandel condition, is solved to determine the effective macroscopic response of the composite material through the process of homogenization. However, the FEM has limitations in terms of computational expenses and numerical complexities. Specifically, when dealing with nonlinear problems, the computational cost significantly increases due to the large number of iterative operations required to obtain an accurate macroscopic response [10].

In recent years, the ROM has emerged as a research hotspot, providing a resolution to the significant computational costs associated with FEM simulation based on the FOM. The ROM enhances computational efficiency by strategically simplifying certain microstructural features and decreasing the degrees of freedom. To date, ROM methods such as Non-Uniform Transformation Field Analysis (NTFA) [11,12], Self-Consistent Cluster Analysis (SCCA) [13], Principal Component Analysis (PCA) [14], Principal Orthogonal Decomposition (POD) [15,16], and Principal Generalized Decomposition (PGD) [17–19] have yielded promising results. While ROMs can achieve acceleration effects ranging from 10 to 100 times, it often encounters a trade-off between accuracy and computational cost when dealing with nonlinear issues. For instance, under nonlinear conditions, NTFA not only requires further refinement of empirical rules but also mandates an extensive exploration of the sampling space, leading to increased computational effort during the offline phase. Although SCCA partially mitigates these limitations of NTFA, it still displays a degradation in accuracy under strong nonlinearity. The POD method, grounded in snapshot technology, defines principal components by employing linear combinations of input variables to predict macroscopic mechanical responses under general load conditions. However, when addressing nonlinear problems, the POD method can exhibit accuracy losses and may even fail under high nonlinearity. To accurately portray nonlinear behavior, the POD method necessitates an increase in snapshot quantity, thereby amplifying the offline computational costs [15]. Apart from ROMs, the fast fourier transform method has also been utilized to augment computational efficiency [20,21]. However, its widespread application remains constrained due to challenges encountered in parallelization [22].

Although most of ROMs can expedite computational efficiency, they are still computationally intensive for homogenization problems, particularly when dealing with nonlinear macro–micro scale coupling issues, resulting in significant computational costs. To improve computational efficiency in the online stage and accuracy under nonlinear conditions, an increasing number of material scientists are attempting to develop data-driven methods. For several decades, simulations and design of heterogeneous materials were commonly based on physical models. However, traditional physical modeling approaches face many challenges when dealing with complex systems. Recently, data-driven methods better address these challenges and enhance efficiency in material design through analysis of existing experimental or simulated datasets. Specifically, in homogenization problems, Yvonnet and colleagues [23] proposed a numerical explicit potential (NEXP) method, which constructs macroscopic constitutive relationships via interpolation of a multitude of sampling points in strain space for nonlinear elastic materials, significantly improving online stage computational efficiency. In recent years, the NEXP has made a further advancements [24,25] and has been applied to topology optimization [26]. However, the vast computational load during the offline stage of the NEXP severely limits its broader application. To tackle this issue, researchers combined the NEXP with ROMs [27], introducing a two-stage data-driven method known as radial NEXP (RNEXP). The RNEXP generalizes to concentric interpolation method [28], substantially reducing offline stage computational costs at the expense of some accuracy, and nearly achieving real-time predictions in the online stage. Nevertheless, it should be noted that if simulations based on ROMs fail, predictions from the RNEXP would also fail. Importantly, the RNEXP is primarily geared towards materials modeled by potential functions, such as hyperelastic materials – the material class of choice in this study – making it well-suited for capturing their behavior. Nonetheless, its applicability may be limited for materials that cannot be succinctly described by strain energy density functions.

In the field of data-driven computational mechanics, machine learning methods receive wide attention, which establishes mappings between the input and output of samples, enabling the rapid assessment of the mechanical properties of composite materials. Presently, various machine learning methods such as artificial neural networks [29–32], support vector machines [33], adversarial neural networks [34], Gaussian regression [35], and convolutional neural networks [36] have yielded impressive results in the field of mechanics. However, it is essential to note that despite their rapid prediction capabilities, these methods might suffer from significant inaccuracies due to limited sample resolution. Additionally, machine learning requires extensive preprocessing of data, leading to high computational costs during the offline stage. Consequently, if the quantity of offline datasets is limited, the precision of the predictions may be compromised. In an attempt to enhance the prediction accuracy of neural network models, Fritzen et al. [37] proposed an adaptive algorithm. This algorithm facilitates an adaptive switch between artificial neural networks and reduced order models, thereby improving prediction accuracy. However, it has to be noticed that under conditions of severe nonlinearity, ROMs might fail, in which condition the accuracy cannot be guaranteed.

Amidst these developments, transfer learning emerges as a novel approach that promises to mitigate some of these issues. Originally a key technique in domains such as image processing, where it has been applied to great effect, transfer learning is now finding its place in computational mechanics. It has been shown to reduce dependence on large volumes of high-fidelity data and thus potentially lower the computational demands associated with machine learning's offline phase [38]. In image processing, for instance, researchers have uncovered through meticulous study that shallow layers of convolutional neural networks usually represent fundamental features such as edges and corners [39]. It has been further revealed that leveraging the general feature extraction ability of pre-trained shallow networks can be advantageous, improving predictive performance while simultaneously reducing the need for extensive domain-specific datasets [39,40]. Yosinski et al. [41] expanded upon this by showing that the success of transferring knowledge from one network to another is influenced by the extent to which layers are adapted or refined. Following the footsteps of image processing, the methodology of transfer learning has been recently extended to the field of computational mechanics, particularly for predicting microstructural properties [42] and analyzing microscopic images [43], with notable success.

This study proposes a transfer learning approach based on the ROM to tackle the challenge of accuracy degradation amidst strong nonlinearity. The scheme progresses through three core stages. To begin with, the ROM is constructed using the data derived from the FOM. Next, the ROM aids in pre-training the neural network structure, and the parameters of the preliminary (or shallow) layers are fixed after pre-training. In the last stage, the parameters of the deep layers are fine-tuned using a limited number of computationally expensive FOM-based simulation results, thereby refining the parameters of the deep network. The incorporation of the transfer learning neural network yields a noteworthy enhancement in prediction accuracy relative to the pre-training network, effectively alleviating the degradation of accuracy in situations dominated by strong nonlinearity. Furthermore, this technique accelerates computations during the online phase and dramatically boosts the computational speed during the offline phase.

The organization of this paper is structured as follows: In Section 2, the hyperelastic homogenization problem is reconceptualized as a minimization problem, with the POD serving as an exemplar of ROMs. The ROM is deployed to generate a substantial volume of dataset for subsequent pre-training. It should be noted that this strategy is applicable to diverse ROM approaches and is not confined to any particular method. The transfer learning approach is introduced in Section 3, where the

network architecture is outlined, and the technique of freezing the fully connected layers is employed as the chosen transfer learning strategy for this investigation. Numerical examples for two-phase hyperelastic materials are presented in Section 4. Finally, conclusions are made in Section 5.

In this work, Voigt notation is introduced for second-order and fourth-order symmetric tensors. This notation permits the conversion of strain and stress from a second-order symmetric tensor into an equivalent first-order tensor (vector). Similarly, the transformation of stiffness, a fourth-order symmetric tensor, into a second-order tensor (matrix representation) is enabled. For the sake of clarity, bold symbols are utilized to represent tensors. Strain and stress are represented by $\boldsymbol{\varepsilon}$ and $\boldsymbol{\sigma}$, respectively, while stiffness is denoted by $\mathbb{C}$. Macroscopic quantities are signified with an overline, such as macroscopic stress $\overline{\boldsymbol{\sigma}}$, macroscopic strain $\overline{\boldsymbol{\varepsilon}}$, macroscopic displacement $\overline{\boldsymbol{u}}$, and macroscopic area $\overline{\boldsymbol{\Omega}}$. Mesoscopic quantities, which are represented without an overline, include mesoscopic stress $\boldsymbol{\sigma}$, mesoscopic strain $\boldsymbol{\varepsilon}$, mesoscopic displacement $\boldsymbol{u}$, and mesoscopic area $\boldsymbol{\Omega}$.

2. Reduced order model

The computational complexity poses a primary challenge when applying the finite element method to computational homogenization problems. In practical engineering applications, particularly in scenarios involving complex microstructures, intricate geometric configurations, various loading conditions, and nonlinear material properties, the extensive degrees of freedom inherent in the finite element method lead to significant computational costs. Hence, the integration of ROMs emerges as a critical approach to mitigate the computational expenses associated with these challenges. By effectively reducing the problem's dimensionality while capturing essential features, ROMs offer a promising avenue to achieve computational efficiency without compromising accuracy in tackling such complex scenarios.

The computational efficiency of the ROM is significantly enhanced by constructing of a reduced-order basis for displacement or strain. Typically, the acceleration efficiency is observed to range from 10 to 100 times, leading to the extensive application of the ROM in the multi-scale simulation of composite materials. Such applications have rendered the ROM a popular surrogate model, especially in the context of dissipative and pseudoplastic materials [27,44]. In the present study, the ROM approach as utilized in [27] was employed, wherein the strain field was decomposed using the POD method for order reduction. It is important to note that the currently developed strategy, built upon the transfer learning method, is not confined to a specific order reduction technique.

The development of the present order-reduction method with POD is based on an energy perspective, through which the corresponding formulas can be derived. It is assumed that the composite material studied contains two phases (r): a hard material and a soft matrix material, which correspond to $r = 1$ and $r = 2$, respectively, and the free energy density is denoted as $W_r(\varepsilon)$. As a result, the corresponding stress and stiffness of phase r can be defined as

$$\boldsymbol{\sigma}^r = \frac{\partial W^r(\boldsymbol{\varepsilon})}{\partial \boldsymbol{\varepsilon}}, \qquad \mathbb{C}^r = \frac{\partial^2 W^r(\boldsymbol{\varepsilon})}{\partial \boldsymbol{\varepsilon}^2}. \tag{1}$$

In order to calculate the effective properties of the RVE according to the homogenization theory, it is necessary to define the averaging operator:

$$\langle \cdot \rangle = \frac{1}{|\Omega|} \int_{\Omega} \cdot dV. \tag{2}$$

The calculation of the average free energy density $\overline{W}(\overline{\varepsilon})$ first requires the definition of the characteristic function $\mathcal{X}^r(\boldsymbol{x})$ of the phase r in the region Ω as follows:

$$\mathcal{X}^r(\boldsymbol{x}) = \begin{cases} 1 & \boldsymbol{x} \in \Omega^r \\ 0 & \boldsymbol{x} \notin \Omega^r \end{cases}, \tag{3}$$

where the spatial region of phase r is denoted as Ω^r. Therefore, the average free energy density $\overline{W}(\overline{\varepsilon})$ in the region Ω can be expressed as

$$\overline{W}(\overline{\boldsymbol{\varepsilon}}) = \frac{1}{|\Omega|} \int_{\Omega} \mathcal{X}^r(\boldsymbol{x}) W^r(\boldsymbol{\varepsilon}(\boldsymbol{x})) dV. \tag{4}$$

Ultimately, the macro-scale effective stress $\overline{\boldsymbol{\sigma}}$ and stiffness $\overline{\mathbb{C}}$ required for the calculation of macro problems can be defined as

$$\overline{\boldsymbol{\sigma}} = \frac{\partial \overline{W}(\overline{\boldsymbol{\varepsilon}})}{\partial \overline{\boldsymbol{\varepsilon}}}, \qquad \overline{\mathbb{C}} = \frac{\partial^2 \overline{W}(\overline{\boldsymbol{\varepsilon}})}{\partial \overline{\boldsymbol{\varepsilon}}^2}. \tag{5}$$

The free energy density must satisfy the following equation according to the principle of energy minimization,

$$\delta \overline{W}(\overline{\boldsymbol{\varepsilon}}) = 0 \Rightarrow \delta \int_{\Omega} \mathcal{X}^r(\boldsymbol{x}) W^r(\boldsymbol{\varepsilon}(\boldsymbol{x})) dV = 0. \tag{6}$$

Note that the present method diverges from the traditional POD approach by decomposing the microscopic strain fluctuation field instead of the displacement field. The microscopic strain field $\boldsymbol{\varepsilon}$ can be decomposed into mean strain $\overline{\boldsymbol{\varepsilon}}$ and fluctuating strain $\widetilde{\boldsymbol{\varepsilon}}$. Consequently, the approximated reduced order solution can be written as

$$\boldsymbol{\varepsilon} = \overline{\boldsymbol{\varepsilon}} + \widetilde{\boldsymbol{\varepsilon}} = \overline{\boldsymbol{\varepsilon}} + \boldsymbol{E}\,\boldsymbol{\xi}, \tag{7}$$

where E is the reduced order basis obtained through the snapshot proper orthogonal decomposition, and $\boldsymbol{\xi}$ is the corresponding coefficient vector for the reduced order basis. The coefficients $\boldsymbol{\xi}$ that minimize the energy can be solved using the Newton–Raphson iterative method. As a result, the macroscopic stress $\overline{\boldsymbol{\sigma}}$ of the ROM is given by

$$\begin{aligned} \overline{\boldsymbol{\sigma}} &= \frac{\partial \overline{W}(\overline{\boldsymbol{\varepsilon}})}{\partial \overline{\boldsymbol{\varepsilon}}} \\ &= \frac{1}{|\Omega|} \int_{\Omega} \mathcal{X}^r(\boldsymbol{x}) \frac{\partial W^r(\overline{\boldsymbol{\varepsilon}} + \boldsymbol{E}\boldsymbol{\xi})}{\partial \boldsymbol{\varepsilon}} dV \\ &= \frac{1}{|\Omega|} \int_{\Omega} \mathcal{X}^r(\boldsymbol{x}) \boldsymbol{\sigma}^r(\boldsymbol{\varepsilon}(\boldsymbol{x})) dV = \langle \boldsymbol{\sigma} \rangle. \end{aligned} \tag{8}$$

The effective tangent stiffness can be calculated using the following expression:

$$\overline{\mathbb{C}} = \frac{d\overline{\boldsymbol{\sigma}}}{d\overline{\boldsymbol{\varepsilon}}} = \langle \mathbb{C} \rangle - \boldsymbol{\Sigma}^T \cdot \boldsymbol{J}^{-1} \cdot \boldsymbol{\Sigma} \tag{9}$$

with

$$\boldsymbol{J} = \langle \boldsymbol{E}^T\ \mathbb{C}\ \boldsymbol{E} \rangle, \qquad \boldsymbol{\Sigma} = \langle \boldsymbol{E}^T\ \mathbb{C} \rangle. \tag{10}$$

The quality and effectiveness of the ROM highly depend on the quality and quantity of high-fidelity snapshots, as well as the number of reduced basis vectors. Therefore, it is essential to carefully choose an appropriate snapshot sampling strategy to ensure a high-quality ROM. In this study, a uniform direction sampling strategy was adopted, which aligns with the sampling strategy commonly employed for training sets in neural network models.

3. ROM-based transfer learning approach

ROMs are extensively employed for computational acceleration. Yet, due to the inherently high computational cost of multiscale computation, a more efficient surrogate model is typically required for practical engineering computations. Recent studies [31,32] suggest that employing artificial neural networks as surrogate models can further enhance computational efficiency. However, machine learning methods necessitate large datasets for training, and resorting to the FOM for data generation results in prohibitive computational expenses. Therefore, this work proposes a transfer learning strategy based on ROMs, significantly reducing the size of datasets generated by the FOM, while effectively mitigating the loss in accuracy of ROMs under strong nonlinear conditions.

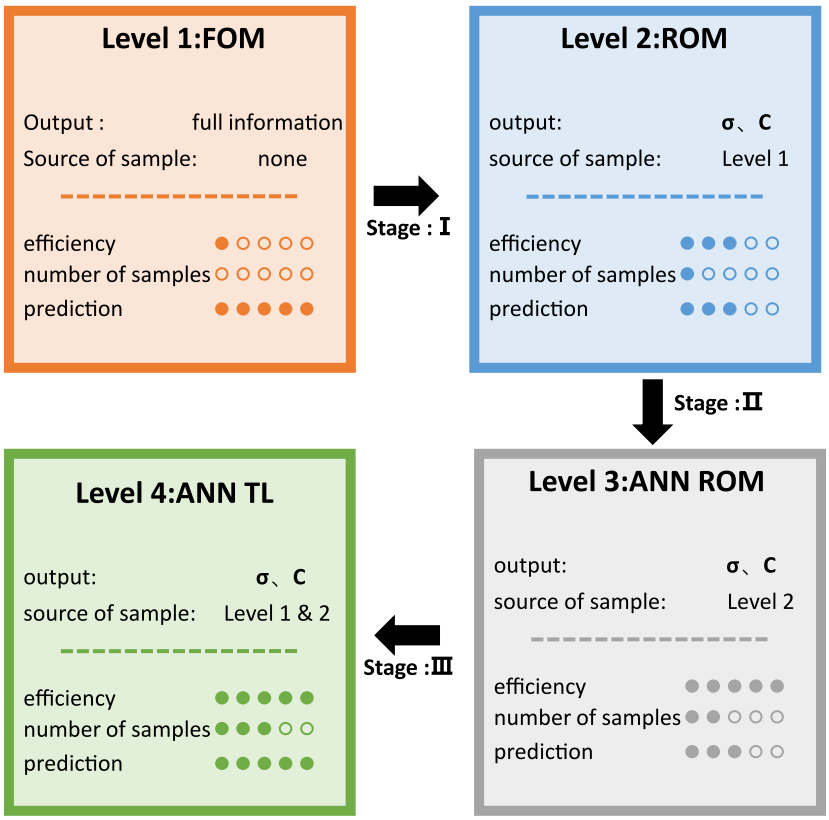

Fig. 1. Transfer learning strategy.

3.1. Four-level surrogate models

In order to rapidly evaluate the microstructural mechanical properties of composite materials, Four-level surrogate models, based on the ROM and the transfer learning strategy, were developed in this work. These four levels include: the FOM, the ROM, a pre-trained artificial neural network model (ANN_ROM) and a calibrated neural network model (ANN_TL). As depicted in Fig. 1, each level has its unique strengths and weaknesses, affording an opportunity to maximize the computational efficiency and prediction accuracy.

- Level 1(FOM): the numerical FE solution of the RVE is obtained under given boundary conditions using the FOM, serving as the accurate solution and benchmark for assessing the accuracy of solutions from the surrogate models.
- Level 2(ROM): the reduced basis is generated based on the FOM, upon which the ROM is established. The POD method was employed in the present study, although our method is not confined to a specific type of ROM, as detailed in Section 2.
- Level 3(ANN_ROM): a vast quantity of data is efficiently generated via the ROM, providing valuable data resources for pre-training the neural network, despite these data potentially being of slightly lower precision.
- Level 4(ANN_TL): the pre-trained neural network is further fine-tuned using a limited amount of high-precision FOM data.

The entire process can be divided into three stages: the generation of the ROM based on the FOM in the first stage; the generation of the ANN_ROM through pre-training the neural network with a large amount of ROM data in the second stage; and fine-tuning the ANN_ROM to obtain the ANN_TL using a limited amount of FOM data in the third stage. During transfer learning, a similarity between the source domain and target domain is required. In this context, the ROM dataset and FOM dataset are fundamentally similar, thereby naturally satisfying the requirements for transfer learning. Additionally, in the calculations of FOM and ROM, the entire load range must be covered to avoid underfitting results. To enable the ROM to adequately cover the entire load space, and considering the high sensitivity of the prediction model to low strain, a non-uniform sampling strategy was implemented. This strategy increases sampling density at low strain amplitudes but assumes a uniform distribution of sampling points in the direction space. Fig. 2 presents a detailed illustration of the specific steps of the transfer learning strategy employed in the present study. It reveals that compared to the FOM, a greater number of load sampling points are considered in the ROM, ensuring the quality of the pre-training model. Moreover, during the transfer learning process, pre-training the neural network is initially conducted in the source domain, followed by the calibration and fine-tuning of the deep network parameters in the target domain, with the shallow network parameters frozen.

3.2. Construction of surrogate model

To simplify the problem, this work focuses on a two-dimensional plane strain problem. To differentiate between the datasets obtained from the ROM and the FOM, the superscript "ROM" is added to the dataset obtained from the ROM.

3.2.1. Network architecture

In the macro–micro scale coupling nonlinear multiscale computations, considerable iterations utilizing the Newton–Raphson method are generally necessary, potentially invoking many millions of times of RVE to evaluate the effective stress–strain constitutive relationships at the micro scale. Resorting to the FOM, it would impose tremendous computational costs. To mitigate this issue, this study opted for the feed-forward neural network architecture as a surrogate model to minimize computational load as much as possible. Although recurrent neural networks(RNNs) outperform feed-forward neural networks in handling historical dependency issues, they bear a higher training cost

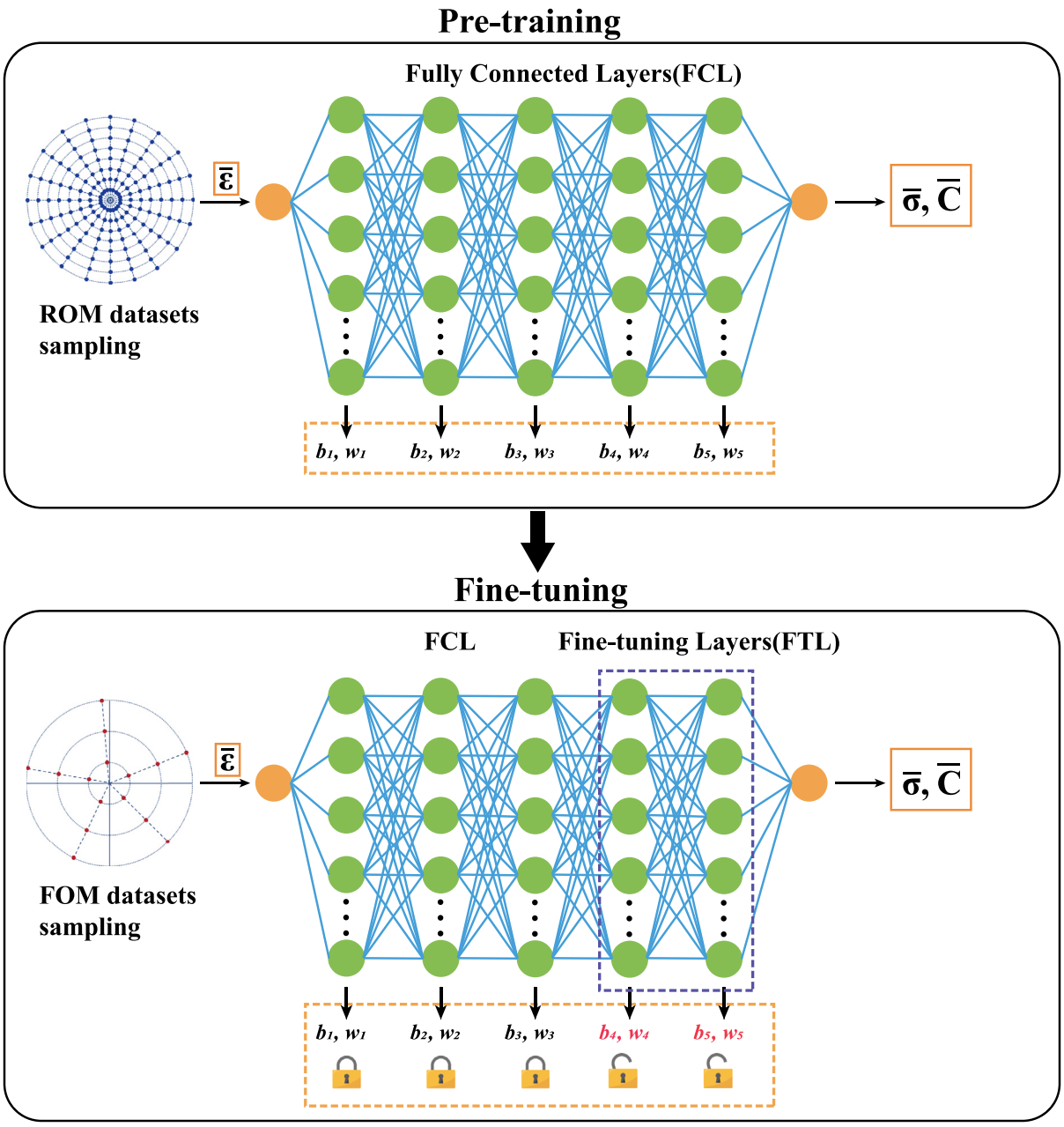

Fig. 2. Diagram of transfer learning.

and demand numerous input paths rather than sampling points for model training. However, for the hyperelastic material problem under investigation in this study, the output of the surrogate model only depends on the effective strain under the current state, independent of the loading history. Therefore, a feed-forward neural network satisfactorily fulfills the requirements while maintaining a relatively lower computational cost.

In the application of neutral network algorithms, the input and output quantities generally need to be normalized to remove the scale effect. The Z-score normalization method was employed in our work for this purpose. Specifically, the following formula was used to normalize the input vector $\bar{\varepsilon}_{ij}$,

$$\tilde{\bar{\varepsilon}}_{ij} = \frac{\bar{\varepsilon}_{ij} - mean(\bar{\varepsilon}_j)}{Std(\bar{\varepsilon}_j)}, \qquad (j = 1, 2, 3, 4), \tag{11}$$

where $\tilde{\bar{\varepsilon}}_{ij}$ represents the standardized macro-scale strain, $\bar{\varepsilon}_{ij}$ denotes the jth macro-scale strain component of the ith sample point, $mean(\bar{\varepsilon}_j)$ and $Std(\bar{\varepsilon}_j)$ represent the mean and standard deviation of the jth macro-scale strain component in the training dataset, respectively. The output quantity $\bar{\sigma}_{ij}$ can also be normalized in a similar way,

$$\tilde{\bar{\sigma}}_{ij} = \frac{\bar{\sigma}_{ij} - mean(\bar{\sigma}_j)}{Std(\bar{\sigma}_j)}, \qquad (j = 1, 2, 3, 4). \tag{12}$$

3.2.2. Generation of datasets

In the present transfer learning approach, two datasets (the source domain and the target domain) were generated. The source domain was obtained by performing extensive sampling through the ROM, while the target domain was generated by sampling using the FOM.

To improve the efficiency of sampling while ensuring comprehensive coverage of the sampling space, the method proposed in [27] was employed in this study. As suggested by Fritzen et al. [27], this method is particularly adept at capturing the directional dependency of the constitutive response. It also addresses the heightened sensitivity to strain amplitudes, especially noticeable at lower levels. In this approach,

the coordinates of the strain sampling points are segregated into two parts: direction and amplitude, which are independently described. Thus, unique sampling methods could be selected for the above two function spaces, providing an improved sampling outcome. For the strain direction sampling, the electrostatic repulsion effect is simulated on a high-dimensional sphere to acquire uniformly distributed sampling points in the strain direction, leading to N_{dir} strain directions $N_j^{\epsilon}, j = 1, 2, \ldots, N_{dir}$, as per [27]. Detailed information on the strain direction sampling method is available in [28]. For strain amplitude sampling, a non-uniform method was employed, resulting in N_{amp} strain amplitudes $E_k, k = 1, 2, \ldots, N_{amp}$. A simple geometric series with parameters R and $\overline{E}_{\max}$ was used in the amplitude sampling as follows, enabling the capture of strain dependence at low amplitudes.

$$\overline{E}_{k+1} = \overline{E}_k + \Delta\overline{E}_{k+1}, \qquad (k = 1, 2, \ldots, N_{amp}), \tag{13}$$

where $\Delta\overline{E}_{k+1}$ is the sampling amplitude increment that can be further written as

$$\Delta\overline{E}_{k+1} = (1 + R)\Delta\overline{E}_k, \qquad (k = 1, 2, \ldots, N_{amp}), \tag{14}$$

when k is set to 1, $\Delta\overline{E}_1$ is equal to $\overline{E}_1$. Furthermore, $\overline{E}_{N_{amp}}$ equals $\overline{E}_{max}$ when k is set to N_{amp}.

Finally, The strain corresponding to the ith sampling point can be expressed as a combination of amplitude and direction as follows.

$$\overline{\varepsilon}_i = \overline{E}_k N_j^{\epsilon} \tag{15}$$

In a two-dimensional plane strain problem, the component form of the strain can be expressed as:

$$\overline{\varepsilon} = (\overline{\varepsilon}_{11}, \overline{\varepsilon}_{22}, \overline{\varepsilon}_{33}, \overline{\varepsilon}_{12}) \tag{16}$$

$\overline{\varepsilon}_{11}, \overline{\varepsilon}_{22}$ represent the normal strain in the x, y direction, $\overline{\varepsilon}_{33}$ represent the normal strain in the z direction and is assumed to be 0 in plane strain condition, $\overline{\varepsilon}_{12}$ represents the shear strain in the x–y plane. The dataset from the source domain, consisting of all the sample points obtained from the ROM, is denoted as D_{ε}^{ROM},

$$\begin{aligned} D_{\varepsilon}^{ROM} = \{\overline{\varepsilon} \in \mathbb{R}^4 \ : \ \overline{\varepsilon} = \overline{E}_k N_j^{\epsilon}, \\ k = 1, 2, \ldots, N_{amp}^{ROM}, j = 1, 2, \ldots, N_{dir}^{ROM}\} \end{aligned} \tag{17}$$

where N_{amp}^{ROM} and N_{dir}^{ROM} denote the numbers of amplitude and direction sampled from the ROM, respectively. The total number of sample points in the source domain is denoted by $\#D_{\varepsilon}^{ROM}$,

$$\#D_{\varepsilon}^{ROM} = N_{amp}^{ROM} \times N_{dir}^{ROM} \tag{18}$$

Similarly, the FOM dataset is represented as D_{ε}^{FOM} and its total number of sample points is denoted as $\#D_{\varepsilon}^{FOM}$. Additional information about these parameters will be presented in the subsequent sections.

3.2.3. Pre-training neural network

A neural network architecture comprising n+2 layers was developed in this work, where the first layer serves as the input layer, the final layer as the output layer, and the others as fully-connected layers. For the ith layer of the fully connected layers, given that the number of its neurons is $L^{(i)}$, the input vector is $\boldsymbol{x}^{(i-1)} \in \mathbb{R}^{L^{(i-1)}}$, the output vector is $\boldsymbol{x}^{(i)} \in \mathbb{R}^{L^{(i)}}$, the weight vector is $\boldsymbol{w}^{(i)} \in \mathbb{R}^{L^{(i)} \times L^{(i-1)}}$, the activation function is $a^{(i)}$, and the bias term is $\boldsymbol{b}^{(i)} \in \mathbb{R}^{L^{(i)}}$, the output of this layer can be represented as follows,

$$\boldsymbol{x}^{(i)} = a^{(i)}(\boldsymbol{w}^{(i)} \ \boldsymbol{x}^{(i-1)} + \boldsymbol{b}^{(i)}). \tag{19}$$

For the overall neural network structure, the input is $\boldsymbol{x}^{(1)} = \widetilde{\overline{\varepsilon}}$ and the output is $\boldsymbol{x}^{(n+2)} = \widetilde{\overline{\sigma}}$. In the macro–micro coupled multiscale computation, besides the computation of RVE's equivalent stress, equivalent stiffness information needs to be provided. In this work, the perturbation method was employed to solve the tangent stiffness matrix. Thus, differentiable activation functions are preferred. The present activation function $a^{(i)}$ uses a hyperbolic tangent function $tanh(x)$, achieving the neural network's fitting of nonlinear data [23]. During the pre-training process, the weight parameters $\boldsymbol{w}^{(i)}$ and bias parameters $\boldsymbol{b}^{(i)}$ are derived by solving an unconstrained optimization problem. Note that the optimization algorithm relies on the chosen optimizer. The optimizer adopted in this work is "Adam", a variant of stochastic gradient descent algorithms that can adjust the learning rate dynamically, which is a popular optimizer for neural networks. Its pre-training process is similar to training a standard artificial neural network. By training the neural network with the "Adam" optimizer, a set of parameters pre-trained based on the ROM data (weights $\boldsymbol{w}_{ROM}^{(i)}$ and biases $\boldsymbol{b}_{ROM}^{(i)}$), i.e., ANN_ROM network parameters, can be obtained. If these parameters were used for direct prediction, the results would be almost consistent with those obtained directly using the ROM computation. However, the error might be significant compared to the results based on the FOM computation in strong nonlinear problems.

3.2.4. Fine-tuning neural network

Fine-tuning the neural network within the transfer learning comprises two steps: (a) transferring and freezing the parameters from non-fine-tuning layers; (b) further fine-tuning the parameters in the fine-tuning layers. Given the significant similarity of problem types and data between the source and target domains in the transfer learning practices, parameters from shallow layers in the neural network (i.e., non-fine-tuning layers) exhibit notable transferability. Therefore, the weight parameters $\boldsymbol{w}^{(i)}$ and bias parameters $\boldsymbol{b}^{(i)}$ of layers preceding the mth layer can be transferred and frozen, and only the parameters within the fine-tuning layers require further tuning. This strategy aims to enhance both the generalization capacity and training efficiency of the neural network. Following the transfer learning method, the parameters of the neural network are represented as

$$(\boldsymbol{w}^{(i)}, \boldsymbol{b}^{(i)}) = \begin{cases} (\boldsymbol{w}_{ROM}^{(i)}, \boldsymbol{b}_{ROM}^{(i)}) & i \le m, \\ (\boldsymbol{w}_{transfer}^{(i)}, \boldsymbol{b}_{transfer}^{(i)}) & i > m, \end{cases} \tag{20}$$

where $\boldsymbol{w}_{ROM}^{(i)}$ and $\boldsymbol{b}_{ROM}^{(i)}$ are the pre-trained neural network parameters based on the ROM dataset, while the $\boldsymbol{w}_{transfer}^{(i)}$ and $\boldsymbol{b}_{transfer}^{(i)}$ are the neural network parameters after fine-tuning based on the FOM dataset.

3.3. Error evaluation

To assess the accuracy of predictions from the surrogate model, the accurate solutions $\overline{\boldsymbol{\sigma}}^{FOM}$ derived from the FOM were taken as reference, to which the solutions $\overline{\boldsymbol{\sigma}}^{ANN}$ generated by the neural network model were compared. The test dataset D_{ε}^{TS} was generated by a uniform and random sampling method. The mean squared error (MSE), mean relative norm error (MRNE), and regression coefficient R_{σ}^2 were employed in this study to evaluate the quality of solutions produced by the surrogate model.

$$MRNE = \underset{D_{\varepsilon}^{TS}}{mean}(RNE) \quad = \underset{D_{\varepsilon}^{TS}}{mean}\left(\frac{\|\overline{\boldsymbol{\sigma}}^{FOM} - \overline{\boldsymbol{\sigma}}^{ANN}\|}{\|\overline{\boldsymbol{\sigma}}^{FOM}\|}\right) \tag{21}$$

$$MSE = \underset{D_{\varepsilon}^{TS}}{mean}(SE) = \underset{D_{\varepsilon}^{TS}}{mean}(\|\overline{\boldsymbol{\sigma}}^{FOM} - \overline{\boldsymbol{\sigma}}^{ANN}\|^2) \tag{22}$$

The regression coefficient R_{σ}^2 denotes the concordance between the surrogate model's predicted solution and the full rrder model's reference solution. The regression coefficient will equate to 1, if and only if the surrogate model's predicted solution precisely matches the reference solution in the test dataset.

4. Numerical validation of the surrogate model

4.1. RVE modeling

In this study, a composite material embedded with cylindrical inclusions served as the validation objective. The hyperelastic base material, used in this validation case, is sourced from Fritzen et al.'s work in [27],

Table 1
Amplitude values from nonuniform sampling.

i	1	2	3	4	5	6	7	8	9	10
$\bar{\varepsilon}_i$ [%]	0.0751	0.1692	0.2866	0.4335	0.6170	0.8465	1.133	1.492	1.940	2.500

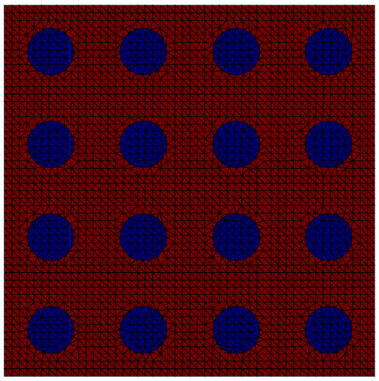

Fig. 3. Cylindrical fibers reinforced RVE.

characterized by its Young's modulus $E = 70000$ MPa, Poisson's ratio $\upsilon = 0.3$, reference strain $\varepsilon_0 = 0.01$, yield stress $\sigma_0 = 100$ MPa, and strain-hardening parameter $p = 0.4$. Elastic material with Young's modulus $E = 400000$ MPa and Poisson's ratio $\upsilon = 0.3$ was utilized as the inclusion. The stress–strain relationship of hyperelastic material is often encapsulated by a strain energy density function, using for defining the material's non-linear elastic property. Within the current RVE model, inclusions occupy a volume fraction of 20%, spread across 16 isotropically distributed spheres. A schematic of the RVE structure is depicted in Fig. 3. The size of the RVE is chosen as 1×1 mm. The meshing of the RVE was carefully designed to be fine enough to capture behavior under large displacements. Periodic boundary conditions were applied to the RVE to obtain more accurate results. It is noteworthy that the proposed method is not confined to the RVE structures and any other materials laws that can be represented by potential functions. Therefore, the size dependency and inclusion number dependency of the RVE will not be elaborated upon in this paper.

4.2. Construction of ROM

In this section, the effectiveness of POD-based reduced order homogenization method for fiber-reinforced composites is investigated. Building upon the sampling strategy outlined in Section 3.2.2, an example for a given number of loading steps $k = 10$, maximum strain amplitude $\bar{\varepsilon}_{max} = 2.5\%$ and constant $R = 0.3$ is given in Table 1.

The construction of ROM is detailed as follows:

- A total $N^{\mathrm{ROM}} = 320$ snapshots were generated with 32 distinct directions and 10 load increments($R = 0.3$) each (cf. Table 1) through finite element simulations based on the high-fidelity RVEs.
- POD technique was applied to the snapshots to extract the reduced bases with various numbers N of strain fluctuation modes for the RVE.
- The ROM was validated along 64 new independent directions with new ten load increments($R = 0.25$), resulting in $N^{\mathrm{ROM}} = 640$ samples of $\overline{\sigma}_{\mathrm{ROM}}$.

Fig. 4(a) illustrates the impact of varying reduced basis mode number N on the accuracy for a representative loading direction $N_{12} = [-0.5771 \quad 0.5921 \quad 0 \quad 0.5624]$. It is evident that as the mode number increases, the predictions of the ROM become more accurate. Notably, with $N = 8$ modes, the model already effectively captures the entire nonlinear response of the system. However, Fig. 4(b) highlights an intriguing phenomenon where the maximum error marginally rises when N escalates from 8 to 256. This increment in error is likely due to the overly oscillatory characteristics of higher-order modes within the POD framework. Such modes, prone to numerical fluctuations, may yield biased basis vectors, adversely impacting the stress response predictions. Therefore, the selection of N is not merely a question of increasing numerical values but involves a strategic consideration of the model's operational dynamics and the desired outcome's accuracy.

Table 2
Network architecture test with 5 layers.

Model ID	Layers (L)	Neurons/Layer	Activation function	MRNE	R^2
ANN_FOM	5	16	RELU	0.5892	0.9727
	5	32	RELU	0.3753	0.9870
	5	64	RELU	0.6599	0.9516
	5	128	RELU	0.6324	0.8864
	5	16	SP	0.4579	0.9775
	5	32	SP	0.2612	0.9824
	5	64	SP	0.2551	0.9813
	5	128	SP	0.5353	0.9811
	5	16	TANH	0.2232	0.9911
	5	32	TANH	0.1152	0.9905
	5	64	TANH	0.0692	0.9991
	5	128	TANH	0.0852	0.9811
ANN_ROM	5	16	RELU	0.4999	0.9989
	5	32	RELU	0.3288	0.9996
	5	64	RELU	0.2292	0.9998
	5	128	RELU	0.5175	0.9999
	5	16	SP	2.0799	0.9879
	5	32	SP	1.9829	0.9880
	5	64	SP	1.4700	0.9988
	5	128	SP	1.0893	0.9993
	5	16	TANH	0.2541	0.9996
	5	32	TANH	0.2016	0.9999
	5	64	TANH	0.1541	0.9999
	5	128	TANH	0.0873	0.9999

4.3. ROM-based transfer learning

4.3.1. Network architecture

Although the accuracy of ROM is acceptable as discussed in Section 4.2, in order to fully explore the proposed transfer learning strategy, the least accuracy of ROM with mode $N = 3$ is specifically selected to generate the ANN training dataset.

The strain space was sampled as described in Section 3.2.2. The FOM dataset was sampled with parameters $N_{dir}^{FOM} = 32$ and $N_{amp}^{FOM} = 5$, resulting in $\#D_{\varepsilon}^{FOM} = N_{amp}^{FOM} \times N_{dir}^{FOM} = 160$ data points. Similarly, the ROM dataset was sampled with parameters $N_{dir}^{ROM} = 512$ and $N_{amp}^{ROM} = 25$, resulting in a total of $\#D_{\varepsilon}^{ROM} = N_{dir}^{ROM} \times N_{amp}^{ROM} = 12800$ strain data points as the input of network-training. The amplitude series parameters for generating the input strain of FOM and ROM datasets were set to $R = 0.3$ and $\bar{\varepsilon}_{max} = 0.025$. Crucially, a validation dataset, constituting 20% of the total data (i.e., $0.2N_{dir}^{ROM}$ and $0.2N_{dir}^{FOM}$, rounded up to the nearest integer), was reserved for model tuning and validation purposes. In addition, a test dataset D_{ε}^{TS} was generated to evaluate the accuracy of the surrogate model. The number of sample directions in the test dataset was $N_{dir}^{TS} = 256$, and the number of sample amplitudes in each direction was $N_{amp}^{TS} = 25$, resulting in a total of $\#D_{\varepsilon}^{TS} = N_{amp}^{TS} \times N_{dir}^{TS} = 6400$ data points. The directions of test dataset were sampled by a uniform and random sampling method. The amplitudes sampling method of the test dataset is similar to FOM and

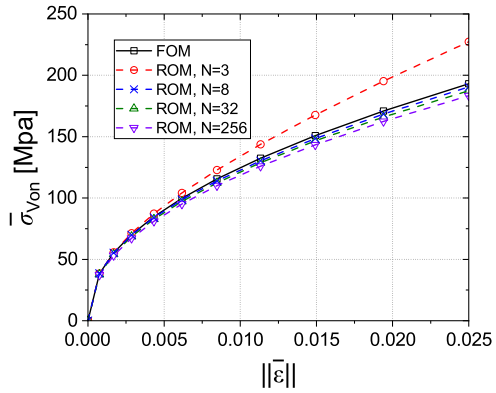

(a) Von-mises stress comparison between FOM and different modes of ROMs.

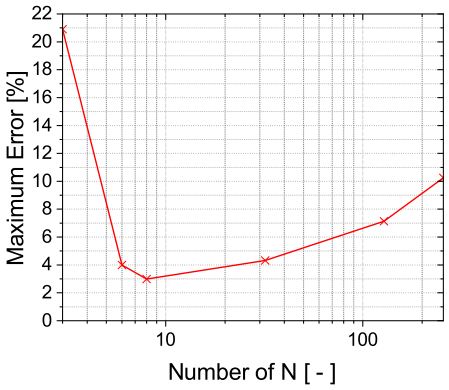

(b) Error comparison between various number of reduced basis modes N.

Fig. 4. Comparison between FOM and ROMs.

Table 3
Network architecture.

ANN ID	FCL × $L^{(i)}$	N^{ROM}_{dir}	N^{ROM}_{amp}	N^{FOM}_{dir}	N^{FOM}_{amp}	FTL	Loss function
ANN_FOM	5 × 64	–	–	32	5	–	mae
ANN_ROM	5 × 128	512	25	–	–	–	mae
ANN_TL	5 × 128	512	25	32	5	1	mae

Table 4
Representative direction in the test dataset (dirTS).

Direction ID	$\bar{\varepsilon}_{11}$	$\bar{\varepsilon}_{12}$	$\bar{\varepsilon}_{33}$	$\bar{\varepsilon}_{22}$
dirTS	−0.6557	0.6252	0	−0.4231

ROM dataset but the series parameters of the test dataset was set to $R = 0.25$ and $\bar{\varepsilon}_{max} = 0.025$ for unbiased comparison.

In order to illustrate the potential of the proposed ROM-based transfer learning strategy, three different ANN models: ANN_FOM, ANN_ROM, and ANN_TL, were constructed and trained for comparison. An initial network architecture testing was conducted on the ANN_FOM and ANN_ROM models due to the differing amounts of data available for these models. This testing encompassed the exploration of different architectural parameters, including the number of layers ($L \in 3, \ldots, 8$), the number of neurons per hidden layer ($n^{[i]} \in 16, 32, 64, 128, i \in 1, \ldots, L-1$), and the evaluation of various activation functions (RELU, SP, TANH).

The architecture of the ANN_TL model was designed to be similar to that of ANN_ROM, based on the principles of transfer learning. In our approach, the shallow layers of the ANN_TL were frozen while the deeper layers were subjected to fine-tuning. This decision was based on the understanding that in neural networks, shallow layers generally capture more generic features which are broadly applicable across different tasks, while deeper layers learn features that are more specific to the particularities of the dataset. By freezing the shallow layers, the ANN_TL model leverages the extensive ROM dataset to grasp the general response of the nonlinear material behavior. Simultaneously, the deeper layers are fine-tuned using a smaller, high-fidelity FOM dataset, enhancing prediction accuracy. The implications of these hyperparameters are further discussed in Section 4.5.

Results of 5 layers from the initial architecture tests, which are detailed in Table 2, indicated a notable advantage of the hyperbolic tangent activation function over others. Therefore, based on these results and considering the differentiability properties of the hyperbolic tangent function, which are beneficial for expected monotonic stress behavior and the need for tangent operators in future finite element (FE) multiscale computations, this function was chosen for further investigation.

The optimal architectures for each of the three models are presented in Table 3. These selections were informed by a comprehensive evaluation of performance metrics, taking into account both accuracy and the computational efficiency of the models.

4.4. Prediction results and performance evaluation

As previously stated, macro–micro coupled multi-scale analyses necessitate a substantial amount of RVE computations at the integration points of macro-scale model to derive the corresponding effective stress and tangent stiffness. In this section, a quantitative examination of the prediction accuracy for effective stress will be performed at the microscopic scale, aiming to compare the performance discrepancies among different surrogate models. As for the tangent stiffness, due to the architecture of current ANNs and the differentiability of the chosen activation function, it can be computed through automatic differentiation provided by TensorFlow library at low computational expense.

4.4.1. Predicted effective stress

In the current validation test, an arbitrary strain direction, dirTS (refer to Table 4), was selected from the test dataset to serve as the representative direction for related examination, while applying varied strain magnitudes to explore the prediction trend. Fig. 5(a) demonstrates the predictions of macroscopic Von-Mises equivalent stress by different prediction models under varying strain magnitudes for the aforementioned representative direction. The results reveal that the ANN_ROM, trained on the dataset computed via the ROM, aligns fairly well with the ROM computational results. However, under strongly non-linear circumstances, or when $\|\bar{\varepsilon}\|$ is significantly large, there may be a loss of accuracy or even prediction failure. The ANN_FOM, trained with data computed from the FOM, mitigates this loss to a certain degree, approaching the accurate solution derived directly from the FOM, but a certain predictive error is still inevitable due to the limited volume of data used. Among all prediction models, the ANN_TL model, trained on datasets derived from both reduced and full order models, exhibits the highest accuracy.

Fig. 5(b) presents a comparative analysis of the predictions from various models on the test dataset, utilizing different error evaluation functions. The FOM computational results serve as the reference here. Apart from the results evaluated via the MRNE, all other error functions exhibit a pattern consistent with that depicted in Fig. 5(a). However, it is clear that the ANN_FOM's predictions on the test dataset are slightly inferior to the ROM in terms of the MRNE. This disparity can be ascribed to the choice of input features and the selection of

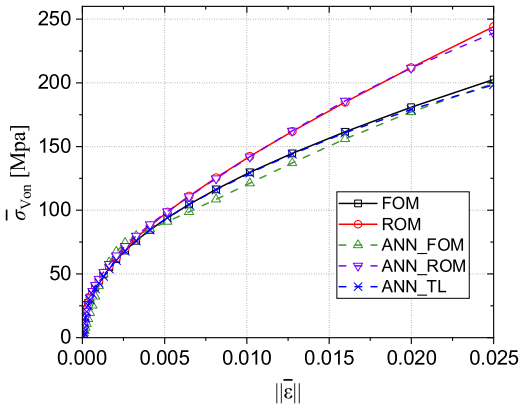

(a) Von-Mises stress vs. strain magnitude.

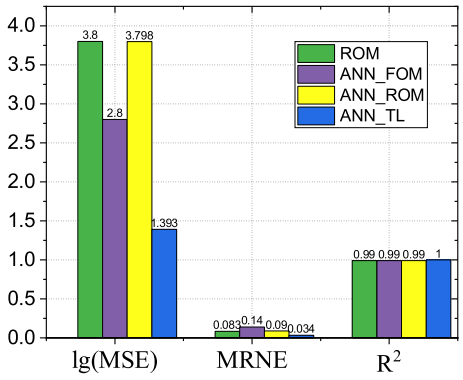

(b) Error assessment based on different error functions.

Fig. 5. Predicted results from various surrogate models on the test dataset in the representative direction dirTS.

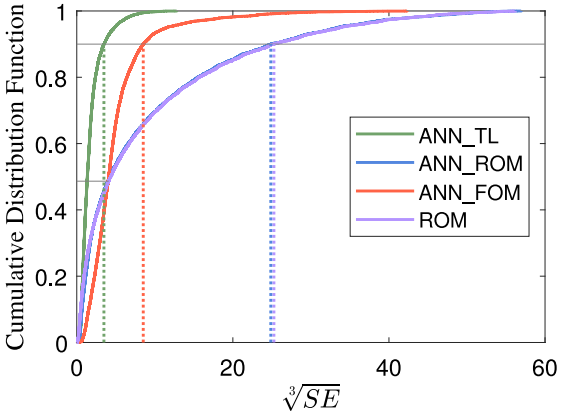

Fig. 6. Cumulative distribution functions of cubed root of standard error (SE) for different surrogate models.

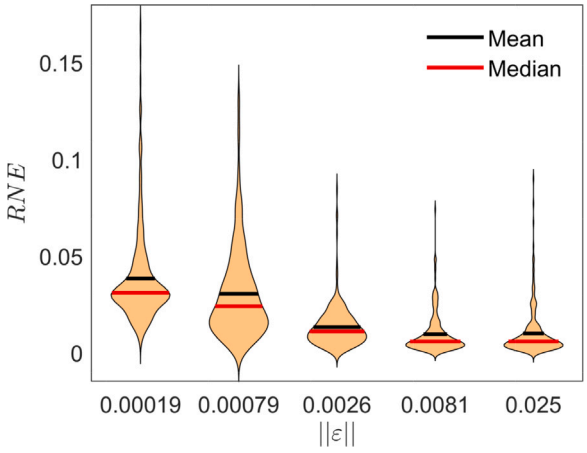

Fig. 7. Distribution of relative norm error in ANN_TL predictions for different strain amplitudes.

loss function within the neural network. Yet, for all error evaluation functions, including MSE, MRNE and R^2_σ, the predictions made by the ANN_TL surrogate model surpass those from other prediction models.

To further understand the error distribution of different prediction models, the error distribution curves obtained by different prediction models are plotted in Fig. 6. From these error curves, it is clear that the ANN_TL surrogate model demonstrates commendable accuracy. The 90% quantile line of the ROM suggests that the upper limit of error in 90% of the sampling points with smaller standard error (SE) from all test dataset is 24.153. This value significantly exceeds the error upper limits of both the ANN_TL and the ANN_FOM, indicating that the prediction accuracy of most sampling points from the ANN_TL and the ANN_FOM far surpasses those of the ANN_ROM and the ROM. Moreover, an intersection at a vertical coordinate of 0.4865 can be noticed between the error curves of the ROM and the ANN_FOM in this figure. This implies that 48.65% of the predictions made by the ANN_FOM surrogate model have errors greater than those of the ROM. This observation validates the need for a more accurate surrogate model, despite the ANN_FOM outperforming the ROM as shown in Fig. 5(a).

The violin plot in Fig. 7 illustrates the distribution of relative norm error (RNE) of different strain magnitudes in the test dataset for the ANN_TL model. It can be observed that despite the presence of significant outliers, i.e., relative norm errors exceeding 0.15, at low strain magnitudes, the majority of the sample points still have relative norm errors less than 0.05. This implies that the predictions of the surrogate model remain accurate in most instances. Furthermore, the error distribution exhibits a higher degree of dispersion at lower strain magnitudes. This is attributed to the heightened sensitivity of macroscopic stress to strain magnitudes at lower strain levels, coupled with a smaller volume of target domain data at the cases of lower strain magnitudes, which can potentially lead to underfitting in the ANN_TL surrogate model.

To visualize the predicted macroscopic stress distribution from the ANN_TL and the ANN_FOM, a comparison is made of the square error distribution scatter plots for both models, as shown in Fig. 8. To facilitate the construction of the scatter plots, a plane with $\varepsilon_3 = 0$ was chosen for sampling, that is to say, sampling point coordinates $\bar{\boldsymbol{\varepsilon}} = (\varepsilon_1, \varepsilon_2, \varepsilon_3, \varepsilon_4) = (\|\varepsilon\| cos(\frac{i}{N_{dir}} 2\pi), 0, 0, \|\varepsilon\| sin(\frac{i}{N_{dir}} 2\pi))$ was adopted, where $i = 1, 2, \ldots, N_{dir}$. The sampling direction number N_{dir} was set to 64, and the amplitude number N_{amp} was 25. A comparison of Figs. 8(a) and 8(b) indicates that the prediction accuracy of the ANN_TL exhibits a significant enhancement over the ANN_FOM. It should also be noted that the maximum square error shown in Fig. 8 predominantly resides in regions of high macroscopic strain amplitude, which aligns with expectations. Furthermore, a symmetric tendency is observed in the overall square error distribution, attributed to the inherent symmetry of the RVE model under investigation in this study.

In order to further investigate the prediction performance of the ANN_TL, the same sampling points used in Figs. 8(a) and 8(b) were retained. Their corresponding relative norm errors were calculated, and scatter plots of these errors were constructed in a similar fashion, the results of which are shown in Fig. 9. The ANN_TL demonstrates

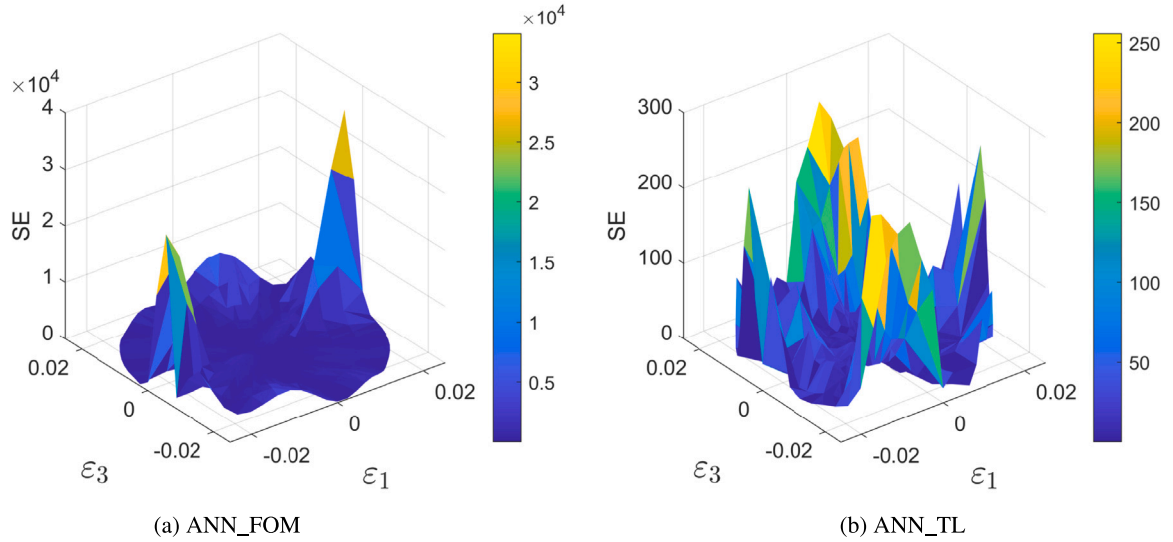

Fig. 8. Squared SE distribution of predicted results from different surrogate models.

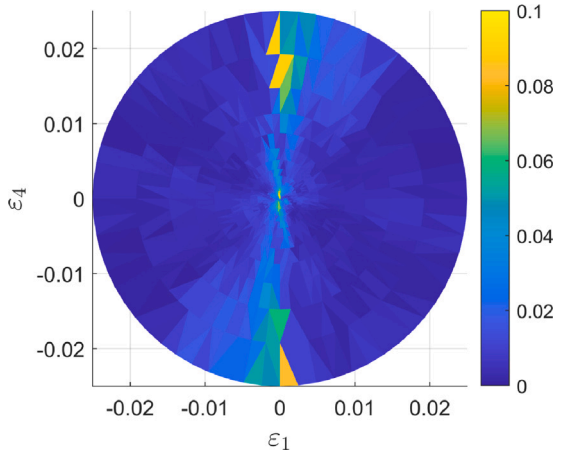

Fig. 9. RNE distribution of macroscopic stress predicted by the ANN_TL on the 2D strain space.

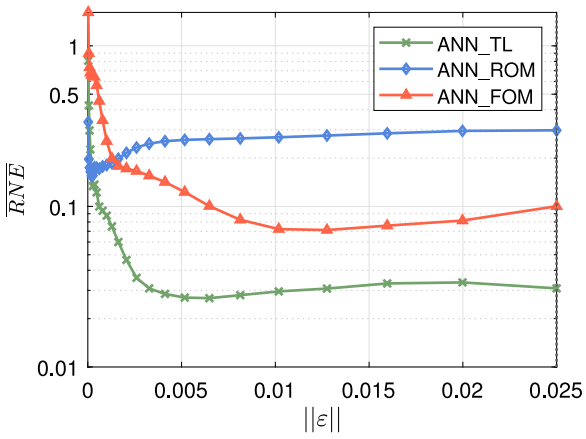

Fig. 10. Average relative norm error $\overline{RNE}$ of prediction results across whole trained domain from different surrogate models.

satisfactory prediction of macroscopic stress in most cases, with relative norm errors predominantly below 0.1. The central minor region, where the relative norm error around 0.1, is predominantly due to the scarcity of input data at lower strain magnitudes. Additionally, from a machine learning perspective, neural network surrogate models are data-driven with no inherent physical principles. The comparative error distribution across the trained domain of the three ANNs was illustrated in Fig. 10. The error metric employed here is the average Relative Norm Error ($\overline{RNE}$), defined as:

$$\overline{RNE} = \frac{1}{N_{dir}^{TS}} \sum_{dir} RNE. \tag{23}$$

Consistent with earlier findings, all models exhibit heightened error rates at very low magnitude inputs. Notably, the ANN_TL model demonstrates a higher sensitivity at these low magnitudes, but the error decreases substantially as the input magnitude increases. In terms of overall error, the ANN_FOM and ANN_ROM models register approximately 10% and 20% errors, respectively. In contrast, the ANN_TL model maintains a lower error rate of about 5%. This result underscores the effectiveness and efficiency of the proposed transfer learning method in the whole trained domain.

4.5. Impact of Hyperparameter on the ANN_TL

4.5.1. Dataset size

In the ANN_TL approach, datasets from the ROM and the FOM serve as the foundation for pre-training and fine-tuning the neural network, respectively. The impact of training data volume on the outcome will be discussed in this subsection. The ANN_TL was tested on a test dataset comprising 256 directional samples, and the regression coefficient R_σ^2, as previously referred to in Section 3.3, was retained as the performance metric. The ROM and FOM datasets' sampling amplitudes were consistently held at $N_{amp}^{ROM} = 25$ and $N_{amp}^{FOM} = 5$. Dataset size varied with the selection of different sampling direction quantities. Consequently, regression coefficient R_σ^2 curves for distinct datasets can be illustrated in Fig. 11. Two key findings regarding N_{dir}^{ROM} and N_{dir}^{FOM} can be derived from Fig. 11 as follows.

For the ROM dataset, a weak correlation exists between the ROM data quantity and predictive accuracy when sampling direction exceeds 50. Due to the neural network's propensity to settle in a local optimum, the regression coefficient curve even might present local decreases. Hence, augmentation of the ROM (source domain) dataset size in the transfer learning will reach a threshold in enhancing predictive accuracy. Furthermore, an enlargement of the FOM dataset corresponds to a less pronounced fluctuation in the regression coefficient R_σ^2, with

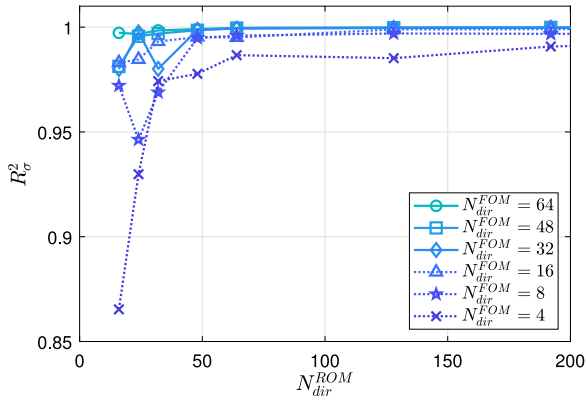

Fig. 11. Regression coefficient R_σ^2 of predicted results using the ANN_TL approach versus the direction number of the dataset.

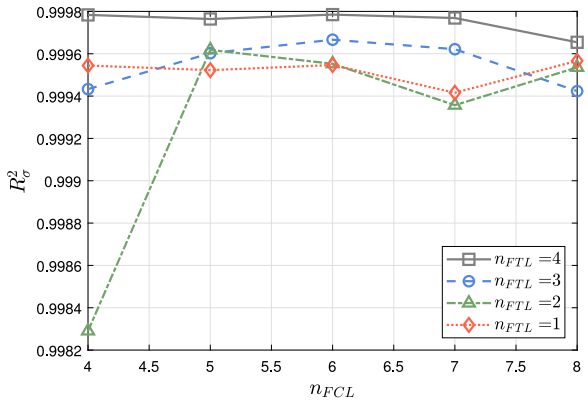

Fig. 12. Influence of n_{FCL} and n_{FTL} on prediction accuracy.

the value nearing 1. This indicates that the prediction performance of the ANN_TL surrogate model improves with the increase of the FOM (target domain) dataset size. However, the impact of the FOM dataset size is also limited when the N_{dir}^{FOM} is larger than 8.

4.5.2. Fine-tuning layer number

In the ANN_TL approach, there are two crucial steps: pre-training and fine-tuning. During the pre-training step, all the fully connected layers (FCLs) are trained, while in the fine-tuning stage, the shallow layers are frozen, and only the parameters in the fine-tuning layer(s) (FTLs) are adjusted. In this section, the influences of the number of fully connected layers (n_{FCL}) and fine-tuning layers (n_{FTL}) on the predicted accuracy are discussed.

Fig. 12 demonstrates the correlation between the regression coefficient of predicted outcomes from the ANN_TL and the numbers of network layers such as n_{FCL} and n_{FTL}. It is evident that neural networks exhibit comparable performance when the total number of fully connected layers ranges between 5 and 7. This implies that in most scenarios, alterations to the number of fully connected layers when exceeding 4 induce minimal impact on the ANN_TL prediction performance. Furthermore, it is generally observed that an increment in the number of fine-tuning layers enhances network prediction accuracy, despite satisfactory accuracy also being achieved at the minimum number of the fine-tuning layers. This phenomenon is attributable to the distinct data qualities of the source and target domains. Hence, from the perspective of improving accuracy of the ANN_TL surrogate model, the pre-trained network parameters are optimally employed as initial parameters, poised for iterative updates utilizing the accurate dataset from the target domain throughout the training process [41]. However, it will increase the network-training cost when increasing the number of the fine-tuning layers.

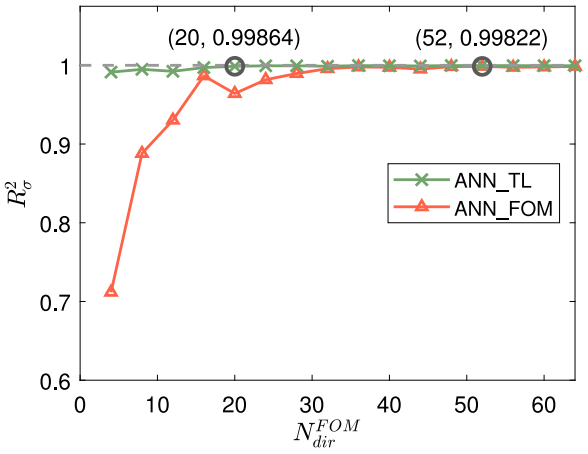

Fig. 13. Comparison of regression coefficients r_σ^2 from ANN_TL and ANN_FOM predictions.

Table 5
Computational cost comparison between ANN_TL and ANN_FOM.

ID	R_σ^2	Numbers of FOM	Numbers of ROM	Time/min
ANN_FOM	0.9986	52 × 25	0	95
ANN_TL	0.9987	20 × 25 + 12 × 5	64 × 5	50

4.6. Discussion on computational cost

As mentioned previously, the current transfer learning approach involves two steps: initially, the ROM generates dataset (source domain) for the initial network training (ANN_ROM), which is then fine-tuned (ANN_TL) using results from the FOM (target domain). However, prior to generating source domain dataset, a small amount of FOM computations are required to derive the ROM. Thus, even though the FOM data volume used for network parameter fine-tuning in the ANN_TL is much less than that used in the direct, single-pass training of neural network to generate a surrogate model (ANN_FOM), the extent of data volume difference between the ANN_TL and the ANN_FOM remains a key concern in this study. This difference directly determines the offline computation cost. Once the neural network training is complete, subsequent online computations yield immediate results, rendering them virtually cost-free in terms of time.

In Section 4.5.1, it has been shown that when the strain directional sampling number of the ROM (N_{dir}^{ROM}) is more than 50, further increases yield negligible performance enhancement for the ANN_TL. At this point, the surrogate model's prediction accuracy primarily relies on the quantity of the FOM dataset ($\#D_\varepsilon^{FOM}$). Hence, in the efficiency comparison between the ANN_TL and the ANN_FOM, the directional sampling number used for pre-training the network is set to $N_{dir}^{ROM} = 64$. To achieve this ROM, a small amount of the FOM data (12 × 5 = 60 data points) was generated. Moreover, to prevent training discrepancies due to variations in the sampled strain amplitude number (N_{amp}), the amplitude sampling numbers were kept consistent in both the ANN_TL and ANN_FOM methods, i.e., $N_{amp}^{FOM} = N_{amp}^{ROM} = 25$. The predictive performance and efficiency differences between the two surrogate models were evaluated by comparing the regression coefficients (R_σ^2) under different strain directional sampling numbers (N_{dir}), as demonstrated in Fig. 13. This figure reveals that the ANN_TL achieves high accuracy with minimal FOM data, whereas the ANN_FOM requires substantially more FOM data and offline computation time. For instance, when comparing data points with similar regression coefficients (R_σ^2) from both the predicted curves (see circled points in Fig. 13), it was found that achieving the same computational accuracy requires nearly double the computational volume for the ANN_FOM in comparison with the ANN_TL, as shown in Table 5. Hence, the ANN_TL

surrogate model considerably reduces the computational demand of the full-order model.

5. Summary and outlook

In homogenization computations of composite materials, traditional numerical methods utilized for evaluating the effective mechanical properties of RVEs necessitate substantial computational resources. Machine learning-based surrogate models, due to their significant reduction in computational cost, have currently gained academic attention. This study introduces a transfer learning strategy integrated with the ROM, which notably lowers the offline computational cost of surrogate models while maintaining predictive accuracy. Given the marginal online computational cost of surrogate models, near-instantaneous results can be acquired, thereby substantially enhancing efficiency in macro–micro scale coupled computations for composite materials and structures.

Evidence indicates that the present method exhibits strong predictive performance. In the offline computational phase of the current validation example, the present approach reduces computational costs by half compared to traditional neural network techniques. Moreover, this transfer learning technique successfully tackles the accuracy loss issue in strong nonlinearity scenarios inherent in the ROM. The present example using the ANN_TL demonstrates an order of magnitude improvement in prediction accuracy compared to the ROM.

Although the proposed method suits for a broad class of hyperelastic materials, it cannot handle real plasticity problems that require correlation with history-dependent loading inputs. This limitation stems from the inherent constraints of the feed-forward neural network architecture. Addressing path-dependent material laws necessitates networks capable of processing sequential data, such as Recurrent Neural Networks (RNNs). Future research can focus on applying similar methods in various types of nonlinear multi-scale simulations [45,46]. Furthermore, by integrating the present method with hyper-reduced methods [47] and hierarchical approximation-based parallel computing [48], computational efficiency in addressing composite materials' problems can be further enhanced.

CRediT authorship contribution statement

Chenyu Nan: Methodology, Software, Writing – original draft. **Hongshi Ruan:** Methodology, Software, Writing – original draft. **Xiaozhe Ju:** Conceptualization, Methodology. **Junhan Hu:** Data curation, Visualization. **Lihua Liang:** Resources, Supervision. **Yangjian Xu:** Conceptualization, Methodology, Writing – review & editing.

Declaration of competing interest

The authors declare that they have no known competing financial interests or personal relationships that could have appeared to influence the work reported in this paper.

Data availability

Data will be made available on request.

Acknowledgments

This work was supported by the National Natural Science Foundation of China (Grant Nos: 52275164 and 12002309) and the Zhejiang Provincial Natural Science Foundation of China (Grant No: LQ21A020002).

References

[1] Jitesh H. Panchal, Surya R. Kalidindi, David L. McDowell, Key computational modeling issues in integrated computational materials engineering, Comput. Aided Des. 45 (2013) 4–25.
[2] G.B. Olson, Computational design of hierarchically structured materials, Science 277 (1997) 1237–1242.
[3] Cahal McVeigh, Franck Vernerey, Wing Kam Liu, L. Cate Brinson, Multiresolution analysis for material design, Comput. Methods Appl. Mech. Engrg. 195 (2006) 5053–5076.
[4] S. Nemat-Nasser, M. Obata, Rate-dependent, finite elasto-plastic deformation of polycrystals, Proc. R. Soc. Lond. Ser. A Math. Phys. Eng. Sci. 407 (1986) 343–375.
[5] P.Ponte Castañeda, The effective mechanical properties of nonlinear isotropic composites, J. Mech. Phys. Solids 39 (1991) 45–71.
[6] P.M. Suquet, Overall potentials and extremal surfaces of power law or ideally plastic composites, J. Mech. Phys. Solids 41 (1993) 981–1002.
[7] J.R. Willis, Upper and lower bounds for non-linear composite behaviour, Mater. Sci. Eng. A 175 (1994) 7–14.
[8] Karel Matouš, Marc G.D. Geers, Varvara G. Kouznetsova, Andrew Gillman, A review of predictive nonlinear theories for multiscale modeling of heterogeneous materials, J. Comput. Phys. 330 (2017) 192–220.
[9] André Zaoui, Renaud Masson, Micromechanics-based modeling of plastic polycrystals: an affine formulation, Mater. Sci. Eng. A 285 (2000) 418–424.
[10] Felix Fritzen, Samuel Forest, Thomas Böhlke, Djimedo Kondo, Toufik Kanit, Computational homogenization of elasto-plastic porous metals, Int. J. Plast. 29 (2012) 102–119.
[11] J.C. Michel, P. Suquet, Nonuniform transformation field analysis, Int. J. Solids Struct. 40 (2003) 6937–6955.
[12] Felix Fritzen, T. Böhlke, Three-dimensional finite element implementation of the nonuniform transformation field analysis, Internat. J. Numer. Methods Engrg. 84 (2010) 803–829.
[13] Zeliang Liu, M.A. Bessa, Wing Kam Liu, Self-consistent clustering analysis: An efficient multi-scale scheme for inelastic heterogeneous materials, Comput. Methods Appl. Mech. Engrg. 306 (2016) 319–341.
[14] Amir Biglari, James C. Sutherland, An a-posteriori evaluation of principal component analysis-based models for turbulent combustion simulations, Combust. Flame 162 (2015) 4025–4035.
[15] J. Yvonnet, Q.-C. He, The reduced model multiscale method (R3M) for the nonlinear homogenization of hyperelastic media at finite strains, J. Comput. Phys. 223 (2007) 341–368.
[16] G. Berkooz, P. Holmes, J.L. Lumley, The proper orthogonal decomposition in the analysis of turbulent flows, Annu. Rev. Fluid Mech. 25 (1993) 539–575.
[17] P. Ladevèze, J.-C. Passieux, D. Néron, The LATIN multiscale computational method and the proper generalized decomposition, Comput. Methods Appl. Mech. Engrg. 199 (2010) 1287–1296.
[18] F. Chinesta, A. Ammar, A. Leygue, R. Keunings, An overview of the proper generalized decomposition with applications in computational rheology, J. Non-Newton. Fluid Mech. 166 (2011) 578–592.
[19] Matthias Leuschner, Felix Fritzen, Reduced order homogenization for viscoplastic composite materials including dissipative imperfect interfaces, Mech. Mater. 104 (2017) 121–138.
[20] Herve Moulinec, Pierre Suquet, A fast numerical method for computing the linear and nonlinear mechanical properties of composites, C. R. Acad. Des Sci. Série II. Mécanique, Phys. Chimie, Astron. (1994).
[21] Nachiketa Mishra, Jaroslav Vondřejc, Jan Zeman, A comparative study on low-memory iterative solvers for FFT-based homogenization of periodic media, J. Comput. Phys. 321 (2016) 151–168.
[22] M. Frigo, S.G. Johnson, The design and implementation of FFTW3, Proc. IEEE 93 (2005) 216–231.
[23] J. Yvonnet, D. Gonzalez, Q.-C. He, Numerically explicit potentials for the homogenization of nonlinear elastic heterogeneous materials, Comput. Methods Appl. Mech. Engrg. 198 (2009) 2723–2737.
[24] Julien Yvonnet, Qi-Chang He, A non-concurrent multiscale method for computing the response of hyperelastic heterogeneous structures, Eur. J. Comput. Mech. 19 (2010) 105–116.
[25] A. Clément, C. Soize, J. Yvonnet, Computational nonlinear stochastic homogenization using a nonconcurrent multiscale approach for hyperelastic heterogeneous microstructures analysis, Internat. J. Numer. Methods Engrg. 91 (2012) 799–824.
[26] Liang Xia, Piotr Breitkopf, Multiscale structural topology optimization with an approximate constitutive model for local material microstructure, Comput. Methods Appl. Mech. Engrg. 286 (2015) 147–167.
[27] Felix Fritzen, Oliver Kunc, Two-stage data-driven homogenization for nonlinear solids using a reduced order model, Eur. J. Mech. A Solids 69 (2018) 201–220.
[28] Oliver Kunc, Felix Fritzen, Generation of energy-minimizing point sets on spheres and their application in mesh-free interpolation and differentiation, Adv. Comput. Math. 45 (2019) 3021–3056.
[29] Larry Manevitz, Akram Bitar, Dan Givoli, Neural network time series forecasting of finite-element mesh adaptation, Neurocomputing 63 (2005) 447–463.

[30] Huanbo Weng, Cheng Luo, Huang Yuan, ANN-aided evaluation of dual-phase microstructural fabric tensors for continuum plasticity representation, Int. J. Mech. Sci. 231 (2022) 107560.
[31] B.A. Le, J. Yvonnet, Q.-C. He, Computational homogenization of nonlinear elastic materials using neural networks, Internat. J. Numer. Methods Engrg. 104 (2015) 1061–1084.
[32] Bin Li, Xiaoying Zhuang, Multiscale computation on feedforward neural network and recurrent neural network, Front. Struct. Civil Eng. 14 (2020) 1285–1298.
[33] Zhihao Jin, Guangdong Chen, Zhengxin Yang, Rolling bearing fault diagnosis based on WOA-VMD-MPE and MPSO-LSSVM, Entropy 24 (2022) 927.
[34] Julien Stöcker, Alexander Fuchs, Ferenc Leichsenring, Michael Kaliske, A novel self-adversarial training scheme for enhanced robustness of inelastic constitutive descriptions by neural networks, Comput. Struct. 265 (2022) 106774.
[35] Kai Zhou, Ryan Enos, Dong Xu, Dianyun Zhang, Jiong Tang, Hierarchical multi-response Gaussian processes for uncertainty analysis with multi-scale composite manufacturing simulation, Comput. Mater. Sci. 207 (2022) 111257.
[36] Huanbo Weng, Yangjian Xu, Junjun Chen, Hongshi Ruan, Chenyu Nan, Lihua Liang, Xiaozhe Ju, An enhanced greedy algorithm for failure resistant material design with application to composite delamination, Compos. Struct. 278 (2021) 114681.
[37] Felix Fritzen, Mauricio Fernández, Fredrik Larsson, On-the-fly adaptivity for nonlinear twoscale simulations using artificial neural networks and reduced order modeling, Front. Mater. 6 (2019) 75.
[38] Sebastian Thrun, Is learning the n-th thing any easier than learning the first? in: Advances in Neural Information Processing Systems, 1995.
[39] Matthew D. Zeiler, Rob Fergus, Visualizing and understanding convolutional networks, in: Computer Vision–ECCV 2014, 2014, pp. 818–833.
[40] Jeff Donahue, Yangqing Jia, Oriol Vinyals, Judy Hoffman, Ning Zhang, Eric Tzeng, Trevor Darrell, Decaf: A deep convolutional activation feature for generic visual recognition, in: International Conference on Machine Learning, 2014, pp. 647–655.
[41] Jason Yosinski, Jeff Clune, Yoshua Bengio, Hod Lipson, How transferable are features in deep neural networks? in: Advances in Neural Information Processing Systems, 2014.
[42] Yangjian Xu, Huanbo Weng, Xiaozhe Ju, Hongshi Ruan, Junjun Chen, Chenyu Nan, Jing Guo, Lihua Liang, A method for predicting mechanical properties of composite microstructure with reduced dataset based on transfer learning, Compos. Struct. 275 (2021) 114444.
[43] Nicholas Lubbers, Turab Lookman, Kipton Barros, Inferring low-dimensional microstructure representations using convolutional neural networks, Phys. Rev. E 96 (2017).
[44] Annika Radermacher, Stefanie Reese, POD-based model reduction with empirical interpolation applied to nonlinear elasticity, Internat. J. Numer. Methods Engrg. 107 (2015) 477–495.
[45] Felix Fritzen, Max Hodapp, The finite element square reduced (FE2r) method with GPU acceleration: towards three-dimensional two-scale simulations, Internat. J. Numer. Methods Engrg. 107 (10) (2016) 853–881.
[46] Matthias Rambausek, Felix Selim Göküzüm, Lu Trong Khiem Nguyen, Marc-André Keip, A two-scale FE-FFT approach to nonlinear magneto-elasticity, Internat. J. Numer. Methods Engrg. 117 (2018) 1117–1142.
[47] D. Ryckelynck, L. Hermanns, F. Chinesta, E. Alarcón, An efficient 'a priori' model reduction for boundary element models, Eng. Anal. Bound. Elem. 29 (2005) 796–801.
[48] Christian Himpe, Tobias Leibner, Stephan Rave, Hierarchical approximate proper orthogonal decomposition, SIAM J. Sci. Comput. 40 (2018) A3267–A3292.